High Power Laser Science and Engineering, (2024), Vol. 12, e10, 9 pages.
doi:10.1017/hpl.2023.93

HIGH POWER LASER SCIENCE AND ENGINEERING

RESEARCH ARTICLE

Synchronized off-harmonic probe laser with highly variable pulse duration for laser–plasma interaction experiments

J. Hornung[1], Y. Zobus[1], H. Lorenté[2], C. Brabetz[1], B. Zielbauer[1], and V. Bagnoud[1,3]

[1] *GSI Helmholtzzentrum für Schwerionenforschung GmbH, Darmstadt, Germany*

[2] *Institut d'Optique, Université Paris-Saclay, Palaiseau, France*

[3] *Institut für Angewandte Physik, Technische Universität Darmstadt, Darmstadt, Germany*

(Received 25 September 2023; revised 9 November 2023; accepted 22 November 2023)

Abstract

This paper presents the development and experimental utilization of a synchronized off-harmonic laser system designed as a probe for ultra-intense laser–plasma interaction experiments. The system exhibits a novel seed-generation design, allowing for a variable pulse duration spanning over more than three orders of magnitude, from 3.45 picoseconds to 10 nanoseconds. This makes it suitable for various plasma diagnostics and visualization techniques. In a side-view configuration, the laser was employed for interferometry and streaked shadowgraphy of a laser-induced plasma while successfully suppressing the self-emission background of the laser–plasma interaction, resulting in a signal-to-self-emission ratio of 110 for this setup. These properties enable the probe to yield valuable insights into the plasma dynamics and interactions at the PHELIX facility and to be deployed at various laser facilities due to its easy-to-implement design.

Keywords: interferometry; laser–plasma interaction; off-harmonic probe laser; streaked shadowgraphy

1. Introduction

A prerequisite for laser–plasma interaction experiments is a precise control of the plasma conditions[1–3]. To optimize this control, accurate measurements of the on-shot plasma properties and dynamics are essential. In particular, the pre-ionization of the target and the following expansion of the plasma due to the temporal-contrast imperfections of the laser play a predominant role, especially in laser–ion acceleration[4,5] or the generation of surface high harmonics[6].

The simulation of such scenarios covering the entirety of the interaction is challenging due to the vast spectrum of phenomena that can be observed over different time scales and intensity regimes. This involves low-intensity, nanosecond-duration scenarios of amplified stimulated emission (ASE), as well as a rapid increase of intensity in the multi-picosecond to femtosecond time scale, due to temporal-contrast features such as pre-pulses, the picosecond-pedestal or the main pulse itself[7]. These extreme ranges of intensities in combination with strong spatial and temporal gradients render the performance of simulations that can cover all scenarios difficult. Existing simulation approaches specialize in specific time and intensity domains, such as particle-in-cell (PIC)[8] and hydrodynamic simulations[9], which can also be combined in so-called hybrid-codes[10,11]. However, performing full-time-scale 3D simulations requires a high amount of computing power and access to a high-performance computing cluster. In this context, experimental measurements offer a complement to simulations while bridging gaps between specialized simulation codes. As a consequence, integrating experimental data into simulations enables understanding laser–plasma interactions, as well as validating and extending our theoretical models. Various techniques, such as interferometry or shadowgraphy using short, sub-picosecond laser pulses or streaked shadowgraphy to measure the dynamics of the plasma on a nanosecond timescale, offer the means to deliver such an input[12,13].

However, performing such measurements is difficult and either requires a laser pulse with a short or long duration, depending on the setup[13]. While some facilities use a leakage of the main laser pulse as a probe beam, this approach usually does not allow for an adaptable pulse duration. Furthermore, the acquired signal is accompanied

Correspondence to: J. Hornung, GSI Helmholtzzentrum für Schwerionenforschung GmbH, Planckstraße 1, 64291 Darmstadt, Germany. Email: j.hornung@gsi.de

by a substantial self-emission background from the scattered light of the main laser pulse[14,15]. Even frequency conversion of the probe beam does not resolve this problem entirely, as the interaction of the main laser pulse with the plasma generates harmonics, contributing to a strong background when probing the interaction region[14,15].

This interfering effect can be reduced by using an off-harmonic probe beam, which eliminates the spectral overlap with the main laser pulse[12]. Traditional methods involve standalone off-harmonic laser systems, which have to be synchronized by electronic timing systems[12], or by frequency shifting a leakage pulse before amplification[16]. Until now, these experimental realizations were limited to a given pulse duration of the probe beam or offered only a small variation of it[12,16].

Therefore, a versatile laser to be used as a plasma probe needs to be synchronized with the main pulse, it must have an off-harmonic center frequency and should preferably have a variable pulse duration to combine it with different detection methods.

In this paper, we report on the development of an optically synchronized, off-harmonic probe laser at the PHELIX facility at the GSI Helmholtzzentrum für Schwerionenforschung in Germany[17], the 'Seeded Experimental Plasma Probe Laser' (SEPPL), which fulfills the above-cited requirements. With the novel idea of utilizing a Fabry–Pérot cavity (FPC) to modulate the seed pulse, this system enables varying the pulse duration from picoseconds up to several nanoseconds, spanning more than three orders of magnitude, using the same source. Since the system is being seeded by components of the main laser chain without interfering with the existing design, it enables a flexible and easy way to set up a synchronized probe laser at various facilities or even enhance the pulse duration range for existing probe laser systems.

2. Principle and setup of the Seeded Experimental Plasma Probe Laser

A scheme of the principle of the SEPPL is shown in Figure 1. The black boxes correspond to the PHELIX beamline, starting from a short-pulse oscillator. A fraction of this pulse feeds an amplifier, providing the energy for the pump pulse of the subsequent ultra-fast optical parametric amplifier (uOPA) stage[18]. Within the following chirped pulse amplification (CPA) chain of the PHELIX facility, the pulse is temporally stretched, amplified and re-compressed before propagating towards the target chamber[17].

The blue boxes indicate the setup of the SEPPL, which runs in parallel to the main laser chain. We generate the seed pulse using a leakage of the ytterbium-doped yttrium aluminum garnet (Yb:YAG)-based uOPA pump laser. In general, the seed can be any leakage of the early stages within the main laser chain. Since the pump pulse within the uOPA process has to be synchronized with the signal

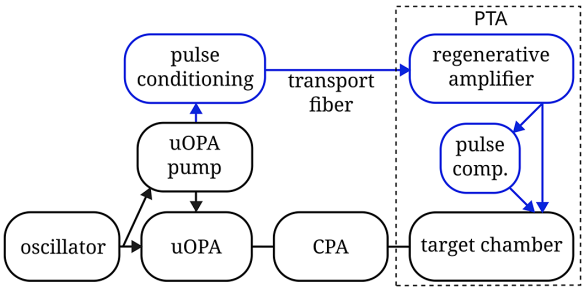

Figure 1. Scheme of the principle of the SEPPL (blue boxes) integrated into the PHELIX facility (black boxes). It shows the main components of the SEPPL, namely the pulse conditioning, amplification, pulse compression and transport of the pulse.

pulse from the initial oscillator, the seed pulse for the SEPPL is automatically synchronized with the main laser pulse. Depending on the required pulse properties, the pulse can be conditioned using an FPC or directly sent to the amplifier. To transport the pulse to the PHELIX petawatt target area (PTA), a polarization-maintaining single-mode fiber is employed, which allows for a flexible position of the probe laser system. The seed pulse enters a linear regenerative amplifier, followed by an optional pulse compressor and frequency-doubling stage, before being transported to the interaction chamber. The principle, setup and relevant properties of the seed generation and the amplification will be detailed in the following.

2.1. Seed generation

The seed-pulse-providing Yb:YAG amplifier delivers pulses with a central wavelength of 1030 nm and a bandwidth of 1 nm, stretched to 275 ps/nm. A more detailed description of this amplifier can be found in Ref. [18]. A leakage with a pulse energy of approximately 10 μJ is sent towards the pulse-conditioning stage, shown in Figure 2. The input pulse can propagate through the FPC to generate long pulses or through a bypass (blue path) before entering the transport fiber.

Using the blue path of the seed, which requires reducing the energy to avoid self-phase modulation within the fiber, the seed can be directly used as the seed for the amplification process.

To create nanosecond pulses, we send the pulse into a FPC consisting of two highly-reflective mirrors in a plano-concave configuration with variable length using a linear translation stage. The first mirror (FlatM) has a reflectivity of (99.8 ± 0.1)% (Layertec 106253), and the second mirror (CavM) has a reflectivity of (99.4 ± 0.3)% (Layertec 101765) with a radius of curvature of 100 mm, placed in a motorized mirror mount. Depending on the reflectivity R_1 and R_2 and distance L between the two mirrors, the FPC only transmits the spectral components of the pulse, which correspond to

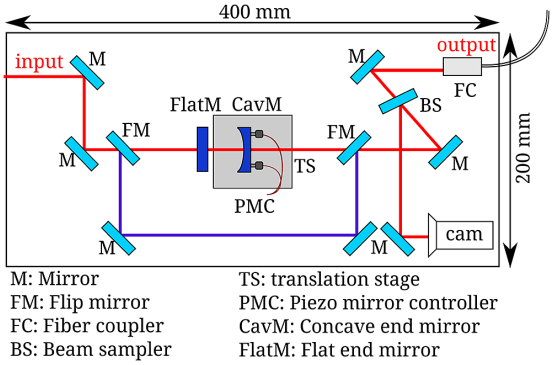

Figure 2. Schematic drawing of the seed-pulse conditioning. The incoming pulse can be sent into the FPC (dark blue mirrors), which can also be bypassed before sending the output pulse into the fiber coupler. In addition, a sample of the FPC transmission is monitored on a camera to control the cavity alignment.

the following frequency:

$$\nu_{qmn} = \frac{c}{2L}\left[q + \frac{m+n+1}{\pi}\operatorname{acos}\sqrt{\left(1-\frac{L}{r_1}\right)\left(1-\frac{L}{r_2}\right)}\right], \tag{1}$$

where c is the speed of light in a vacuum and r_1 and r_2 correspond to the radius of curvature of the cavity mirrors. The integer values q and m, n correspond to the number of longitudinal and spatial modes, respectively[19]. For the case of a Gaussian beam with a spatial TEM_{00} mode, for example, $m,\ n = 0$, this leads to a transmitted spectrum that consists of spectral lines with a distance of $\delta\nu = \nu_{100} - \nu_{000} = c/2L$, which corresponds to the well-known equation of possible longitudinal modes within a cavity. For higher-order spatial modes, the spectral spacing of the possible transmitted components additionally depends on the reflectivity of the FPC, described by the additional term in Equation (1), which will also influence the temporal behavior of the transmitted laser pulse. The strength of each individual longitudinal and spatial mode is not described by this equation and can be tuned by matching the spectral and spatial properties of the incoming laser pulse to the desired modes.

The general temporal shape of the transmitted pulse is given by the cavity ring-down[20], depending on the reflectivity R and transmission T of the mirrors, as well as the length L of the FPC. The pulse with a field amplitude of $E(t)$ performs n round trips within the cavity with a time of $t_r = 2L/c$, where the resulting transmitted intensity $I(t)$, for two mirrors of similar reflectivity, is given by the following:

$$I(t) = T^2 I_0 \left| \sum_{n=0}^{\infty} R^n E\left(t - n t_r\right) \exp\left(i\Phi\right) \right|^2 . \tag{2}$$

The phase term Φ is correlated to the spatial modes of the cavity influenced by Equation (1), which has an influence on the transmission spectrum, leading to fast oscillations within the pulse profile. The resulting transmitted profile has a rapid rise in intensity, correlated to the initial pulse duration, and a much longer exponential tail with a decay time that increases with rising reflectivity of the mirrors and FPC length, resulting in nanosecond-long transmission times.

2.2. *Amplification and compression*

The regenerative amplifier used to amplify the seed pulse shares a common design with the uOPA pump[18]. It runs at a repetition rate of 10 Hz, synchronized with the front end and independent of the full-energy shots of the PHELIX facility. The setup is visible in Figure 3, where the flat and concave mirrors (blue) delimit the linear amplifier cavity. A high-power laser diode (DILAS M1F4S22-940.3-500Q-IS10.23) pumps the Yb:YAG crystal in a 12-pass pump configuration. Multipassing the pump beam in a three-level laser system improves the absorption of the pump without introducing strong losses at the laser wavelength. Using a Yb:YAG crystal, emitting around 1030 nm, avoids spectral overlap between the SEPPL and the PHELIX pulse, which is centered at 1053 nm with a bandwidth of 3 nm (full width at half maximum, FWHM).

After amplification, the Faraday isolator acts as a separator for the backward-propagating laser pulse. A subsequent combination of a wave plate and polarizer allows for tuning of the output energy. At two positions, the output is picked up by a camera to monitor the spatial profile and by a fiber coupler, which sends the pulse to a photodiode and a 4 GHz oscilloscope to monitor the pulse duration and cross-check the delay with the PHELIX main beam.

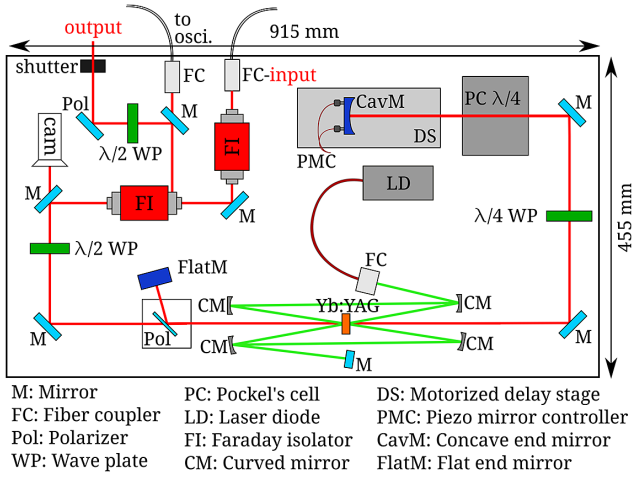

Figure 3. Schematic drawing of the regenerative amplifier with a total size of 915 mm × 455 mm. The input pulse enters the amplifier through a fiber coupler (red input), passes two Faraday isolators and enters the main cavity, delimited by the flat and concave mirrors (blue). The cavity is set up around a Yb:YAG crystal, which is being pumped by a 12-pass pump system, powered by a laser diode.

With this setup, even very low seed pulses with an energy in the nJ range can be amplified up to 7 mJ at a central wavelength of 1030 nm. It has to be noted that it is only possible to use a regenerative amplifier if the seed generation occurs as early as possible within the laser chain in order to synchronize the output with the driving laser pulse. In the case of the PHELIX facility, the main laser pulse is amplified by a regenerative amplifier after the uOPA stage, where the seed is taken from, which allows us to bridge the time difference within the regenerative amplifier.

When bypassing the FPC to amplify chirped pulses in combination with the double-pass pulse compressor, the energy is reduced by 35% but the pulse duration shortens to a few picoseconds. This compressor can also be bypassed, independent of the pulse conditioning. To ensure similar conditions for the short and long pulse configurations for the upcoming performance characterization, the pulse always passes through the compressor after the amplification process.

After amplification and compression, the pulse can also be frequency doubled, which increases the spectral separation between the SEPPL and the PHELIX pulse before guiding it towards the interaction chamber. The distance between the compressor exit and the entrance of the interaction chamber that has to be covered by the beam is approximately 5 m. As the peak power of the amplified pulses may surpass 1 GW, imaging telescopes would need to be placed in a vacuum to avoid plasma generation in the focal spot. In order to reduce the cost of the system, we set up a beamline without imaging, which, however, increases the requirements on the stability of the system.

3. Performance

Since the PHELIX facility is able to deliver a full-energy shot every 90 minutes and has a dead time of up to several minutes before the shot during which no pulse from the main laser chain is available, the stability of the probe laser is crucial for reliable and comparable measurements. These relevant properties will be described in the following section.

3.1. Pulse duration

By sending the amplified and chirped pulse into a folded double-pass grating compressor, it is possible to reduce the pulse duration to (3.45 ± 0.11) ps (FWHM) at 1030 nm, measured by a second-order scanning autocorrelator. The following frequency doubling additionally shortens the pulse, which results in an estimated pulse duration of (2.44 ± 0.08) ps (FWHM) at 515 nm.

Furthermore, we characterized the pulse duration of the nanosecond pulses as a function of the FPC length, which is visible in Figure 4. The measurements of the pulse with

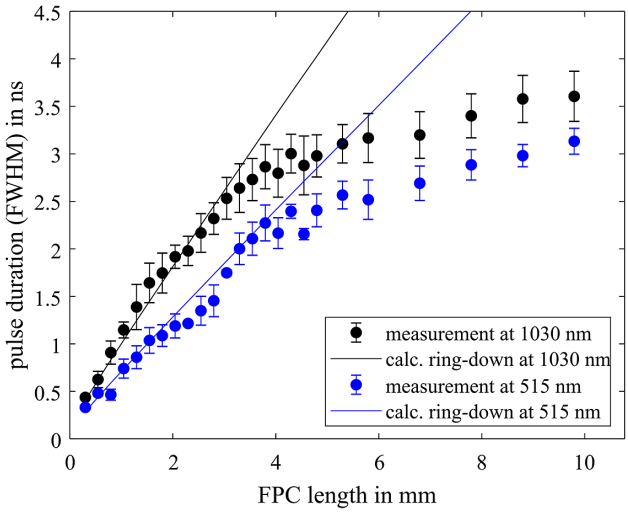

Figure 4. Dependency of the pulse duration at 1030 nm (black) and 515 nm (blue) on the length of the FPC used for the seed generation. The black and blue lines correspond to the calculated pulse duration at central wavelengths of 1030 and 515 nm, respectively, given by the cavity ring-down using a reflectivity of 99.7% for both mirrors.

a central wavelength of 1030 nm (black) were performed using a photodiode with a rise time of 85 ps and a 4 GHz oscilloscope (Tektronix MSO64). The frequency-doubled pulses at 515 nm (blue) were measured using a streak camera (Hamamatsu C10910) with a sweep range of 10 ns and a resolution of 50 ps.

By modulating the seed pulse with the FPC, it is possible to generate pulses with a continuously adjustable pulse duration from 0.4 ns up to 3.5 ns. Note that the pulse duration was measured after the amplification since a measurement of the seed itself, primarily the nanosecond pulse, was not possible due to the very low transmission of the FPC.

The influence of the amplification also manifests itself in the deviation between the measurement and the calculated ring-down time. Due to the amplifier cavity length of 1.4 m and the rise time of the Pockels cell of 3 ns, the maximum pulse duration is limited to approximately 2.75 ns for a full pulse extraction. For a longer seed-pulse duration, the pulse shape becomes distorted. This can, however, still be used to generate longer pulses. By overloading the cavity of the regenerative amplifier, it is possible to transmit two round trips of the cavity at once. This reduces the output energy but increases the possible pulse duration up to 10 ns. Note that the pulse duration reachable by overloading the amplifier cavity is not included in Figure 4.

The measured pulse shapes for a selection of FPC lengths (0.3, 1.3 and 2.3 mm) in combination with the resulting pulse of the overloaded cavity are visible in Figure 5.

The temporal shape of the pulse is given by the behavior of a cavity ring-down with an exponential decay if the input pulse is longer than the FPC[20]. The visible modulations within the pulse shape with a frequency of 1.73 and

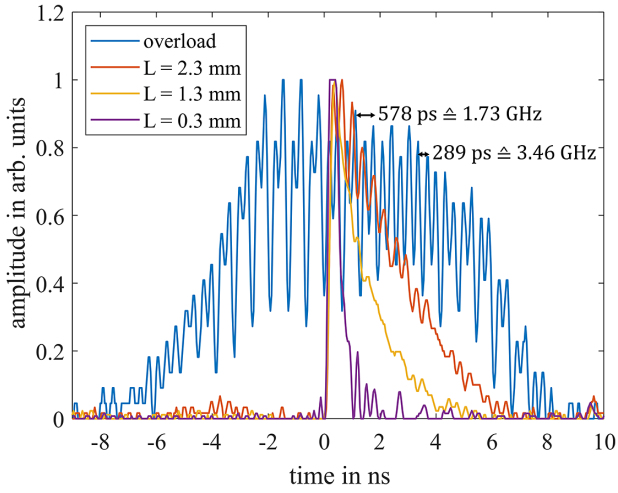

Figure 5. Shape of the pulse duration using FPC distances of 0.3 mm (purple), 1.3 mm (yellow) and 2.3 mm, as well as the resulting pulse using the overload (OL) mode of the amplification cavity (blue).

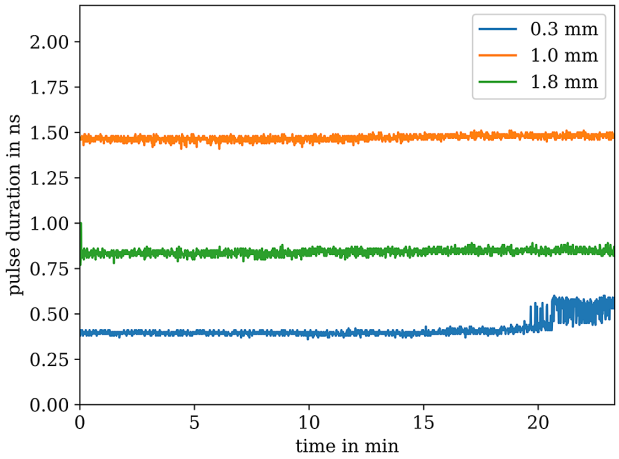

Figure 6. Pulse duration stability over 23 minutes for different FPC lengths. Only the shortest cavity shows a deviation after 10 minutes.

3.46 GHz, respectively, result from mode beating of different higher-order spatial modes with $m,\ n \neq 0$ (see Equation (1))[21]. These modes might arise from the seed itself or from an imperfect coupling into the FPC. The beating of the single longitudinal modes is not visible since the free spectral range for the measured FPC lengths varies between 350 and 10 GHz, which cannot be resolved by the used diagnostics. These modulations also increase the uncertainty of the FWHM pulse duration measurement in Figure 4.

Removing the temporal oscillations would be possible by performing perfect spatial mode matching within the FPC. A possibility to increase the frequency of the modulations beyond the detection limit could be achieved by setting up a confocal cavity where the length of the cavity is equal to the radius of the concave mirrors, which leads to an equidistant frequency spacing for all spatial modes. However, this would eliminate the advantage of pulse duration tuning. Another possibility to increase the oscillation period beyond the pulse duration and therefore reduce the modulation visibility could be achieved by using a flat-concave setup with a long radius of curvature $R_2/L >> 1$.

The setup of the seed generation therefore enables the possibility to change the pulse duration from 3.44 ps to 10 ns by more than three orders of magnitude, enabling different applications for the probe laser.

3.2. Pulse duration stability

The stability of the pulse duration on a short timescale has already been indicated by Figure 4. These measurements of the pulse duration were performed over a duration of 1 minute, showing a peak-to-valley (PtV) uncertainty between 6% for the shortest pulse and 20% for longer pulses, which is mainly dominated by the uncertainty of the fast temporal oscillations.

However, since we are generating the nanosecond pulse with an FPC, which is sensitive to the misalignment of the cavity, we performed a pulse duration stability measurement for different FPC lengths. Figure 6 shows the pulse duration (FWHM) for FPC lengths of 0.3 mm (blue), 1 mm (orange) and 1.8 mm (green). During that time, neither the length nor the cavity mirrors of the FPC were adjusted.

The figure shows that the pulse duration of the longer FPC is stable over the full measurement duration. Only the shortest cavity length shows a deviation in pulse duration, around 20 minutes into operation. This jump corresponds to a gradual decrease in transmission of the FPC due to a small misalignment of the cavity mirror by thermal effects, reducing the signal strength on the photodiode and therefore decreasing the signal-to-noise ratio. The measurement shows that the pulse duration and therefore the FPC are stable enough for operation when performing the realignment close to firing the main laser. In the future, this realignment process can be automated by a feedback loop to the motorized FPC mirror.

3.3. Energy stability

The output energy at the fundamental wavelength is permanently monitored by an output camera of the regenerative amplifier, which is cross-calibrated by a calorimeter (Gentec QE25-SP-S-MB-D0). In addition, we measured the energy and the pointing stability of the frequency-doubled beam inside the target chamber after a free-space propagation of 5 m over a duration of 45 minutes. At 515 nm, this showed a root mean square (RMS) pointing stability of 2.34 µrad (24.04 µrad PtV) and an RMS energy stability of 4.49% (27.82% PtV). As a comparison, the pulse energy at 1030 nm had an RMS stability of 2.03% (11.38% PtV). These measurements show that there is no strong fluctuation in the energy or position of the beam, enabling predictable conditions for the probe laser.

3.4. Timing synchronization

Another critical point is the temporal stability between the main laser pulse and the probe beam. One part of the stabilization occurs at the uOPA front end, since the main pulse and pump pulse have to be synchronized at this position already. This is currently done with a precision of 100 fs. This precision will be increased in an upcoming update of the uOPA. In order to measure the jitter at the PTA, we monitor both pulses with an 8 GHz oscilloscope (Tektronix DPO 70804C), a fast photodiode with a rise time of 18.5 ps (Newfocus 1454) and a streak camera (Hamamatsu C10910) with a 0.5 ns sweep time and a resolution of 2.5 ps. We define the jitter as the variation of the first moment of the temporal pulse distribution at a fixed delay between both pulses. The corresponding jitter measurement, around the initial delay between the pulses, using the streak camera has been performed for a duration of approximately half an hour.

These measurements show an RMS temporal stability of 1.95 ps (PtV 8.99 ps) using the fast photodiode and an RMS of 2.67 ps (PtV 13.13 ps) for the measurement using the streak camera. Since the detectors are much slower than the time difference we want to observe, we performed a cross-check. We repeated this measurement of the timing difference between the PHELIX pulse and a replica with a fixed delay of 300 ps, generated at the beginning of the laser chain. In principle, the timing jitter should be negligible in this configuration, since both pulses propagate along the exactly same beam path and originate from the same source. However, we also found a jitter with an RMS of 1.77 ps (PtV 8.29 ps), measured using the 8 GHz oscilloscope and the fast photodiode, which is very similar to the jitter RMS of 1.95 ps between the SEPPL and the PHELIX pulse. Therefore, we assume that the real timing jitter between both pulses is lower than the measured one. It would be beneficial to repeat these measurements with a detector with a faster response in order to verify that the respective resolution of the detection systems is not the limiting factor.

These measurements also show that the applied delay between these pulses is stable over a long time period. This delay between the main pulse and the SEPPL can be tuned by moving a motorized linear translation stage within the regenerative amplifier of the SEPPL. This allows us to fine-tune the delay to ± 2.3 ns, with a minimal step size of approximately 240 fs, correlated to the number of round trips within the amplifier. It is also possible to introduce much longer delays of approximately ± 200 ns by tuning the number of round trips within the amplifier cavity. However, this would also alter the available energy and energy stability after the amplification.

The initial delay between the PHELIX pulse and the SEPPL has to be measured at the interaction point for every new setup within the target chamber. In order to verify and control the delay after these measurements, we permanently monitor both pulses on a 4 GHz oscilloscope. The PHELIX pulse is picked off at the last sensor of the laser chain before the target chamber. For the SEPPL, we use a fiber-coupled pick-off after the regenerative amplifier, which guides the pulse towards the oscilloscope. This allows for a cross-check of the delay with a precision of less than 70 ps, depending on the used photodiode.

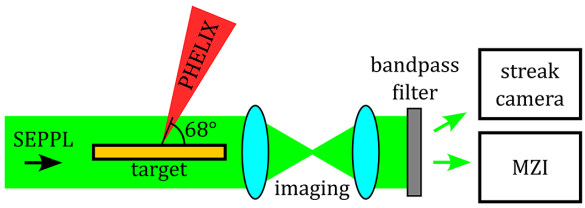

Figure 7. Experimental setup using the SEPPL as a probe laser for the characterization of a preplasma induced by the PHELIX laser. The probe can be sent into an MZI for measuring the density profile or used for streaked shadowgraphy of the plasma expansion.

4. Commissioning at the PHELIX facility

In order to test its performance, the SEPPL was commissioned during an internal beamtime at the PHELIX facility. The corresponding setup to perform a side-viewed measurement of the laser–plasma interaction and expansion is shown in Figure 7. The pump laser hits a gold target of various thicknesses at an angle of 22°, while the SEPPL probes the target parallel to its surface with a spot size of 1.7 ± 0.2 mm perpendicular to the target. It has to be noted that the angle between the PHELIX pulse and the SEPPL is not restricted and can be adapted to match the desired experimental geometry. We irradiated the target either with a nanosecond low-energy pulse emulating the ASE pedestal or with the main laser pulse at maximum energy and a pulse duration of 500 fs, resulting in intensities on-target up to 5×10^{20} W/cm^2 for a spot size of 3.8 µm[22]. The probe laser and the image of the interaction region are guided outside of the vacuum chamber using an imaging system with a total magnification of 10.2 using a first lens with a numerical aperture of 0.25. However, the resolution was limited by the width of the targets (2 mm) in the propagation direction of the SEPPL, resulting in a spatial resolution of approximately equal to 12 µm.

Using two band pass filters with 1 nm (Thorlabs FL514.5-1) and 3 nm (Thorlabs FL514.5-3) bandwidths at 514.5 nm, the transmission at a spectral distance of ± 5, ± 10 and ± 55 nm can be calculated, resulting in a background suppression of 6, 8.5 and 11 orders of magnitude, respectively. This shows that the frequency-doubled PHELIX spectrum, centered at 526.5 nm with a 10 nm spectral offset to the SEPPL spectrum, is also suppressed by 8.5 orders of magnitude.

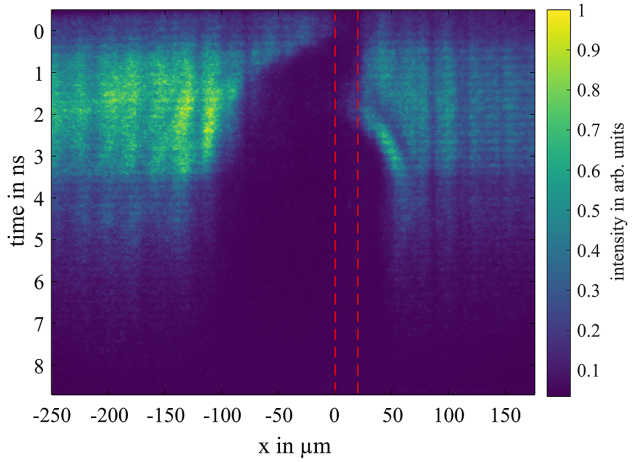

Figure 8. Streaked shadowgraphy of a 20 µm thick gold target located at $x = 0$ µm. The initial position is indicated by the red dashed lines. The laser hits the target at $t = 0$ from the left-hand side, leading to an expansion of the plasma, which is monitored for a duration of almost 10 ns.

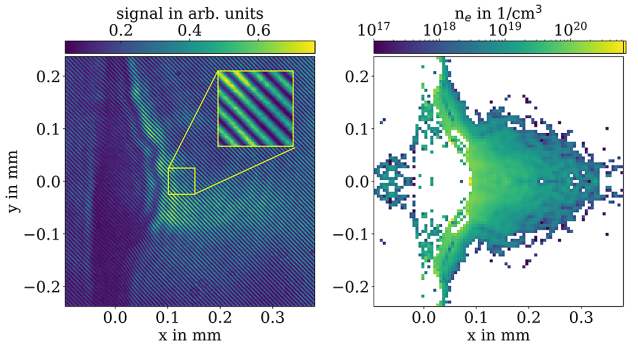

Figure 9. The left-hand side shows an interferometric measurement of a plasma expansion, and the inlet shows a zoomed region of the resulting interference fringes. The right-hand side shows the electron density distribution, extracted from the plasma refractive index of the left-hand side measurement.

Afterwards, the pulse can either be sent into a streak camera or a Mach–Zehnder interferometer (MZI), depending on the measurement setup.

The measurements deploying streaked shadowgraphy were performed using the low-energy nanosecond pulse with a duration of 1 ns and 1 J on-target, focused onto a 20 µm thick gold target to a spot size of 4 µm. The resulting spatial and temporal dynamics of the plasma expansion are shown in Figure 8 over a duration of almost 10 ns (vertical axis) with a temporal resolution of approximately equal to 50 ps. Here the laser hits the target, indicated by the red dashed lines, from the left-hand side at $t = 0$. The probe beam with a pulse duration of 3.2 ns (FWHM) at a central wavelength of 515 nm was temporally shifted by 500 ps before the start of the interaction. The temporal oscillations introduced by mode beating within the FPC are also visible, parallel to the horizontal axis. The black vertical modulations in the spatial profile of the laser are introduced by imperfections on the slit of the streak camera.

Nevertheless, it is possible to track the movement of the critical surface, indicated by the expanding black region, with an initial expansion velocity of up to 150 ± 30 km/s at the front side and a break-out time at the rear side between 1.1 and 2.4 ns, corresponding to a shock velocity of 13 ± 5 km/s.

For an interferometric measurement of the plasma expansion, we switched the pulse duration to 2.44 ps and guided the beam towards an MZI containing a 16-bit camera with a chip size of 13.3 mm × 13.3 mm and a pixel size of 6.5 µm (PCO Edge 4.2). Taking into account the magnification of the imaging system, the interferometric measurement has a field of view of 1.3 mm × 1.3 mm, which is fully covered by the probe beam and still over-saturates the camera at full energy.

By slightly detuning one of the MZI mirrors, we introduced interferometric fringes with an effective spacing of 5.7 µm, visible in the inlet of the left-hand side of Figure 9. This is still smaller than the resolution of the imaging system. It has to be noted that the influence of the temporal smearing, due to the pulse duration of the SEPPL and the expansion of the plasma, has to stay below the mentioned spatial resolution. The smearing is therefore negligible as long as the velocity does not exceed 2.3×10^6 m/s, indicating an upper limit of measurable plasma expansions.

The left-hand side of Figure 9 also shows a measurement of the plasma expansion by an artificial pre-pulse with an energy of 1 J and a duration (FWHM) of 1 ns that introduces a controlled pre-expansion of the target, initially located at $x = 0$ µm. The snapshot was taken 500 ps after the beginning of the interaction. The right-hand side shows the corresponding electron density reconstruction from the interferometric fringes, assuming an axial cylindrical symmetry of the plasma, using an Abel transformation[13]. The white areas correspond to electron densities below 10^{17} cm^{-3}. It can be seen that the maximum measured electron density of approximately equal to 5×10^{20} cm^{-3} is one order of magnitude lower than the theoretical limit, given by the critical density at 515 nm, of 4.2×10^{21} cm^{-3}. This occurs due to a high refraction index close to the critical density, which in turn strongly deviates the beam path of the light rays away from the collecting lens of the imaging system[13]. The white area within the target is also non-physical, since the beam cannot penetrate this region of the target.

In addition, we measured the plasma self-emission by the main laser pulse, without the probe laser, for a pulse energy of 97 J on-target. The self-emission had a peak intensity of 592 counts, compared to the background noise of 108 counts. Since we made use of the full 16-bit range of the camera, this results in a signal-to-background ratio of 110 for this specific experimental setup, which can be even further

enhanced when increasing the energy of the probe beam and additionally introducing neutral density filters.

These examples show that it is possible to perform side-viewed interferometry, shadowgraphy and streaked shadowgraphy of the plasma expansion with a high signal-to-noise ratio using the SEPPL. The interferometric measurement allows one to measure and reconstruct plasma distributions with an electron density ranging from 10^{17} up to 5×10^{20} cm^{-3} at variable delay times. In addition, the nanosecond pulses enable streaked shadowgraphy over a wide range of sweep times to perform temporally resolved measurements of expanding plasmas and break-out times of laser-driven shocks.

5. Conclusion

In summary, we developed a synchronized probe laser for the PHELIX PTA that is able to generate synchronized pulses of variable pulse duration from 3.45 up to 10 ns at 1030 nm, using a plano-concave FPC to modulate the incoming seed pulse. The temporal pulse shape currently shows modulations caused by multiple spatial modes within the cavity, which can be improved by performing proper mode matching or adapting the radius of the curved mirror. The SEPPL is able to deliver pulse energies of up to 7 mJ at 1030 nm and 2 mJ at 515 nm, which has no spectral overlap with the second harmonic of the main drive laser of the PHELIX facility (527 nm). We showed that the probe laser has an RMS temporal stability with the main pulse of at least 1.95 ps, which is limited by the precision of the measurement method. An improved method with a permanent timing measurement between the two pulses[23] could be part of future upgrades to the SEPPL. These characteristics of the SEPPL allowed us to perform side-viewed streaked shadowgraphy and interferometry of a main-beam-driven plasma with a signal-to-self-emission ratio of 110 for the commissioning setup, which can be even further improved by increasing the output energy of the SEPPL and introducing neutral density filters. The commissioned probe laser allows us to increase our understanding of laser–plasma dynamics and interaction at the PHELIX facility, and it will be available to external users for pump-probe experiments. Due to its flexible and easy-to-implement design, this scheme could be deployed at various laser facilities that are missing a probe laser or currently use an on-harmonic pick-off of the main laser chain. It can even increase the range of possible pulse durations of existing probe lasers by utilizing the novel method of using an FPC for seed-pulse modulation.

Competing interests

The authors declare no competing interests.

References

1. M. Nishiuchi, N. P. Dover, M. Hata, H. Sakaki, K. Kondo, H. F. Lowe, T. Miyahara, H. Kiriyama, J. K. Koga, N. Iwata, M. A. Alkhimova, A. S. Pirozhkov, A. Y. Faenov, T. A. Pikuz, A. Sagisaka, Y. Watanabe, M. Kando, K. Kondo, E. J. Ditter, O. C. Ettlinger, G. S. Hicks, Z. Najmudin, T. Ziegler, K. Zeil, U. Schramm, and Y. Sentoku, Phys. Rev. Res. **2**, 033081 (2020).
2. T. Ziegler, D. Albach, C. Bernert, S. Bock, F.-E. Brack, T. E. Cowan, N. P. Dover, M. Garten, L. Gaus, R. Gebhardt, I. Goethel, U. Helbig, A. Irman, H. Kiriyama, T. Kluge, A. Kon, S. Kraft, F. Kroll, M. Loeser, J. Metzkes-Ng, M. Nishiuchi, L. Obst-Huebl, T. Püschel, M. Rehwald, H.-P. Schlenvoigt, U. Schramm, and K. Zeil, Sci. Rep. **11**, 7338 (2021).
3. J.-R. Marquès, P. Loiseau, J. Bonvalet, M. Tarisien, E. d'Humières, J. Domange, F. Hannachi, L. Lancia, O. Larroche, P. Nicolaï, P. Puyuelo-Valdes, L. Romagnani, J. J. Santos, and V. Tikhonchuk, Phys. Plasmas **28**, 023103 (2021).
4. N. P. Dover, T. Ziegler, S. Assenbaum, C. Bernert, S. Bock, F.-E. Brack, T. E. Cowan, E. J. Ditter, M. Garten, L. Gaus, I. Goethel, G. S. Hicks, H. Kiriyama, T. Kluge, J. K. Koga, A. Kon, K. Kondo, S. Kraft, F. Kroll, H. F. Lowe, J. Metzkes-Ng, T. Miyatake, Z. Najmudin, T. Pöschel, M. Rehwald, M. Reimold, H. Sakaki, H.-P. Schlenvoigt, K. Shiokawa, M. E. P. Umlandt, U. Schramm, K. Zeil, and M. Nishiuchi, Light Sci. Appl. **12**, 71 (2023).
5. J. Goodman, M. King, R. Wilson, R. J. Gray, and P. McKenna, New J. Phys. **24**, 053016 (2022).
6. S. Kahaly, S. Monchocé, H. Vincenti, T. Dzelzainis, B. Dromey, M. Zepf, P. Martin, and F. Quéré, Phys. Rev. Lett. **110**, 175001 (2013).
7. V. A. Schanz, C. Brabetz, D. J. Posor, D. Reemts, M. Roth, and V. Bagnoud, Appl. Phys. B **125**, 61 (2019).
8. T. D. Arber, K. Bennett, C. S. Brady, A. Lawrence-Douglas, M. G. Ramsay, N. J. Sircombe, P. Gillies, R. G. Evans, H. Schmitz, A. R. Bell, and C. P. Ridgers, Plasma Phys. Controll. Fusion **57**, 113001 (2015).
9. B. Fryxell, K. Olson, P. Ricker, F. X. Timmes, M. Zingale, D. Q. Lamb, P. MacNeice, R. Rosner, J. W. Truran, and H. Tufo, Astrophys. J. Suppl. Ser. **131**, 273 (2000).
10. S. Fatemi, A. R. Poppe, G. T. Delory, and W. M. Farrell, J. Phys. Conf. Ser. **837**, 012017 (2017).
11. P. A. Muñoz, N. Jain, P. Kilian, and J. Büchner, Comput. Phys. Commun. **224**, 245 (2018).
12. C. Bernert, S. Assenbaum, F. E. Brack, T. E. Cowan, C. B. Curry, M. Garten, L. Gaus, M. Gauthier, S. Göde, I. Goethel, S. H. Glenzer, T. Kluge, S. Kraft, F. Kroll, M. Kuntzsch, J. Metzkes-Ng, M. Loeser, L. Obst-Huebl, M. Rehwald, H.-P. Schlenvoigt, C. Schoenwaelder, U. Schramm, M. Siebold, F. Treffert, T. Ziegler, and K. Zeil, Sci. Rep. **12**, 7287 (2022).
13. D. Batani, J. Santos, P. Forestier-Colleoni, D. Mancelli, M. Ehret, J. Trela, A. Morace, K. Jakubowska, L. Antonelli, D. del Sorbo, M. Manclossi, and M. Veltcheva, J. Fusion Energy **38**, 299 (2019).
14. F. Wagner, S. Bedacht, A. Ortner, M. Roth, A. Tauschwitz, Z. Zielbauer, and V. Bagnoud, Opt. Express **22**, 29505 (2014).
15. K. L. Lancaster, J. Pasley, J. S. Green, D. Batani, S. Baton, R. G. Evans, L. Gizzi, R. Heathcote, C. H. Gomez, M. Koenig, P. Koester, A. Morace, I. Musgrave, P. A. Norreys, F. Perez, J. N. Waugh, and N. C. Woolsey, Phys. Plasmas **16**, 056707 (2009).
16. S. Feister, J. A. Nees, J. T. Morrison, K. D. Frische, C. Orban, E. A. Chowdhury, and W. M. Roquemore, Rev. Sci. Instrum. **85**, 11D602 (2014).
17. B. Bagnoud, B. Aurand, A. Blazevic, S. Borneis, C. Bruske, B. Ecker, U. Eisenbarth, J. Fils, A. Frank, E. Gaul, S. Goette,

C. Haefner, T. Hahn, K. Harres, H.-M. Heuck, D. Hochhaus, D. H. H. Hoffmann, D. Javorková, H.-J. Kluge, T. Kuehl, S. Kunzer, M. Kreutz, T. Merz-Mantwill, P. Neumayer, E. Onkels, D. Reemts, O. Rosmej, M. Roth, T. Stoehlker, A. Tauschwitz, B. Zielbauer, D. Zimmer, and K. Witte, Appl. Phys. B **100**, 137 (2010).

18. Y. Zobus, C. Brabetz, M. Loeser, A. Albach, M. Siebold, and V. Bagnoud, Opt. Express **31**, 5002 (2023).
19. P. W. Milonni and J. H. Eberly, *Laser Physics* (John Wiley & Sons, 2010).
20. J. Y. Lee and H.-W. L. Won Hahn, Jpn. J. Appl. Phys. **38**, 6287 (1999).
21. J. Martin, B. A. Paldus, P. Zalicki, E. H. Wahl, T. G. Owano, J. S. Harris, C. H. Kruger, and R. N. Zare, Chem. Phys. Lett. **258**, 63 (1996).
22. J. Hornung, Y. Zobus, P. Boller, C. Brabetz, U. Eisenbarth, T. Kühl, Zs. Major, J. B. Ohland, M. Zepf, B. Zielbauer, and V. Bagnoud, High Power Laser Sci. Eng. **8**, e24 (2020).
23. T. Ziegler, M. Rehwald, L. Obst, C. Bernert, F.-E. Brack, C. B. Curry, M. Gauthier, S. H. Glenzer, S. Göde, L. Kazak, S. D. Kraft, M. Kuntzsch, M. Loeser, J. Metzkes-Ng, C. Rödel, H.-P. Schlenvoigt, U. Schramm, M. Siebold, J. Tiggesbäumker, S. Wolter, and K. Zeil, Plasma Phys. Control. Fusion **60**, 074003 (2018).